

Balance of actively generated contractile and resistive forces controls cytokinesis dynamics

Wendy Zhang* and Douglas N. Robinson†*

*Department of Physics, James Franck Institute, University of Chicago, Chicago, IL 60637; and †Department of Cell Biology, The Johns Hopkins University School of Medicine, 725 North Wolfe Street, Baltimore, MD 21205

Communicated by James A. Spudich, Stanford University School of Medicine, Stanford, CA, March 28, 2005 (received for review January 3, 2005)

Cytokinesis, the fission of a mother cell into two daughter cells, is a simple and dramatic cell shape change. Here, we examine the dynamics of cytokinesis by using a combination of microscopy, dynamic measurements, and genetic analysis. We find that cytokinesis proceeds through a single sequence of shape changes, but the kinetics of the transformation from one shape to another differs dramatically between strains. We interpret the measurements in a simple and quantitative manner by using a previously uncharacterized analytic model. From the analysis, wild-type cytokinesis appears to proceed through an active, extremely regulated process in which globally distributed proteins generate resistive forces that slow the rate of furrow ingression. Finally, we propose that, in addition to myosin II, a Laplace pressure, resulting from material properties and the geometry of the dividing cell, generates force to help drive furrow ingression late in cytokinesis.

cell dynamics | myosin II | dynacortin | RacE | cell mechanics

How cells form diverse shapes such as extended neurons or columnar epithelium or change shape during movement is an important mystery in cell biology. Cytokinesis, the mechanical separation of a mother cell into two daughter cells, is a simple shape change that is essential for cell viability. Its failure can lead to defects in cell growth and aneuploidy, causing diseases such as cancer.

Cytokinesis is coordinated by the mitotic spindle, which delivers cues to the actin-rich cortex. These cues lead to a redistribution of a number of cytoskeletal proteins, including myosin II, to the cell's equator (1). In the classic model, myosin II constricts an equatorial actin ring, producing two daughter cells (2–6). Puzzlingly, cytokinesis in some cell types proceeds fairly normally without myosin II. Other observations suggest that both the polar/global and equatorial regions of the cell cortex have important roles in the contractile process (7–11). Thus, cytokinesis appears to be executed by a complex network, involving multiple force-generating systems and regulatory feedback loops. Consequently, many proteins may contribute important functions to cytokinesis without producing gross phenotypes when mutated (12). However, at present, we know very little about how the entire cytokinesis machinery works.

Here, we analyze the time dependency of furrow ingression of wild-type and mutant *Dictyostelium* cytokineses by measuring the furrow diameter and length and applying an appropriate rescaling strategy. This method reveals, in a noninvasive way, features distinctive of each strain. In all cell types, cytokinesis proceeds through essentially the same sequence of shapes. However, the kinetics of transformation between shapes differs dramatically between wild-type and mutant strains. We analyzed the role of equatorial proteins, myosin II and the actin crosslinker cortexillin I, and global proteins, RacE small GTPase and the actin crosslinker dynacortin (Fig. 1A). Each protein plays an important role in cytokinesis and cortical mechanics (7, 13–18). Each mutant strain follows a unique time-dependent trajectory of furrow ingression. By comparing the data with a quantitative model, the cylinder thinning model, we propose that myosin II-generated active radial stresses, a Laplace pressure

generated from material properties and RacE/dynacortin-generated resistive stresses, govern furrow-thinning dynamics. With this combination of genetics and cell imaging and modeling, a quantitative framework in which molecular mechanisms are related to cytokinesis dynamics becomes possible.

Materials and Methods

Strains. All genetic strains used in this study have been described in refs. 15 and 19–21. Wild-type cells were HS1000 cells (19). Control strains carried the parental plasmid, pLD1A15SN, which allowed all cells to be grown under identical media conditions (19). To generate the *RacE/dynacortin* and *myosin II/dynacortin* double-mutant combinations, *RacE* and *myosin II* mutant strains were transformed with a *dynacortin* hairpin (*dynhp*) construct (15). No dynacortin protein was detectable in *dynhp* cells by Western immunodetection by using anti-dynacortin antibodies as described and quantified in ref. 15.

Microscopy. Log-phase *Dictyostelium* cells were plated in imaging chambers. Because temperature can impact physical parameters such as viscosity, the imaging temperature was standardized to $22 \pm 0.5^\circ\text{C}$. Cells were imaged with a $\times 40$ oil, NA1.3 objective and a $\times 1.6$ optivar. UV, IR, and green filters were used to eliminate phototoxicity. Frames were collected every 2 s until the intercellular bridge was severed by using the IP LAB software package (Scanalytics, Billerica, MA). The time-lapse movies were analyzed by using NIH IMAGE (<http://rsb.info.nih.gov/nih-image/Default.html>), Microsoft EXCEL, and KALEIDAGRAPH (Synergy Software, Reading, PA).

Results

Wild-Type Furrows Constrict Exponentially. To initiate our analysis, we studied the dynamics of wild-type cytokinesis and defined two phases of shape progression (Fig. 1B; see also Movies 1 and 2, which are published as supporting information on the PNAS web site). During phase 1, the mother cell rounds up, elongates into a cylinder, and forms a cleavage furrow that links up smoothly with the daughter cells (Figs. 1B and 2B). Although the shape of the polar cortex is variable because of ruffling, the shape in the furrow region always appears taut. During phase 2, the cleavage furrow cortex constricts until a discrete bridge is formed. The cell now appears more dumbbell-shaped, and the bridge is a geometrically separate structure from the two daughter cells. The bridge thins out as a result of cytoplasmic flow from the bridge before severing. Typically, the scission point is located near one of the daughter cells instead of in the middle of the bridge. After breakup, the bridge rapidly recoils into the daughter cell to which it is connected. In short, the entire sequence of shape changes can be described as a transformation from one geometrically simple shape to another: from a single sphere to two spheres connected by a cylinder to two daughter spheres.

Abbreviations: LTM, laser-tracking microrheology; MPA, micropipette aspiration.

†To whom correspondence should be addressed. E-mail: dnr@jhmi.edu.

© 2005 by The National Academy of Sciences of the USA

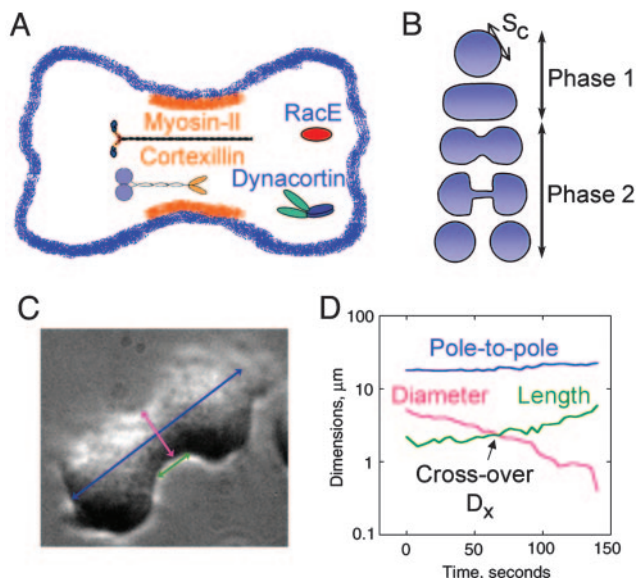


Fig. 1. The shape changes of cytokinesis. (A) Schematic cartoon showing localizations of myosin II, RacE, dynacortin, and cortexillin I. (B) A cartoon of the shape changes of wild-type cytokinesis. The break between phase 1 and phase 2 indicate the predicted transition state of furrow ingression (18). (C) A phase micrograph of a wild-type cell in cytokinesis. The furrow diameter (pink arrow), furrow length (green arrow), and the pole-to-pole (blue arrow) were monitored with 4-s resolution for each cell. (D) An example plot from a wild-type cell showing how the dimensions changed with time. The crossover point, D_x , is indicated.

To see which aspects of the detailed cytokinesis dynamics are robust, we averaged measurements from individual cells so that the same stage of division in different cells is reliably correlated. We measured the minimum furrow diameter and furrow length as a function of time (Fig. 1 C and D). To measure the furrow length, we defined the furrow as the region where the sides of the bridge were parallel (i.e., the cylindrical portion). During late stages, typically when the furrow diameter is approximately $\leq 4 \mu\text{m}$, the length is completely objective, whereas during early stages, the furrow has more curvature, making the cylindrical portion somewhat more subjective. For these early stages, we defined the length as the most cylindrical portion to the region in which the divergence angle from the long axis of the cell was approximately $< 25^\circ$. From the diameter and length vs. time plots, we observed that for every cell, there was a time point when the minimal furrow diameter and furrow length were equal; we defined this distance as the crossover distance, D_x . The crossover time was reset to 0, and D_x was reset to 1. The remaining furrow diameters were divided by D_x . Because D_x is a constant, the division does not affect the kinetics of furrow thinning but allows the trajectories to collapse onto a universal trajectory (Fig. 3). To verify the success of rescaling, nonaveraged data were analyzed before being averaged for curve fitting and further analysis (Fig. 3; see also Fig. 6, which is published as supporting information on the PNAS web site). The rescaling allowed the kinetics of cytokinesis for a large number of cells across a variety of genotypes to be compared. For wild type, the furrow diameters decayed nonlinearly and were best described as an exponential trajectory with $k = -0.012 \text{ s}^{-1}$ (Fig. 3A).

RacE and Dynacortin Provide a Brake. To analyze how globally distributed RacE and dynacortin (19, 22, 23) control furrow ingression dynamics, we studied two *RacE* mutant lines (an insertional mutant, *RacE*^{24E}, and a deletion line, Δ *RacE*; ref. 20) and *dynacortin* mutants generated by silencing *dynacortin* with a

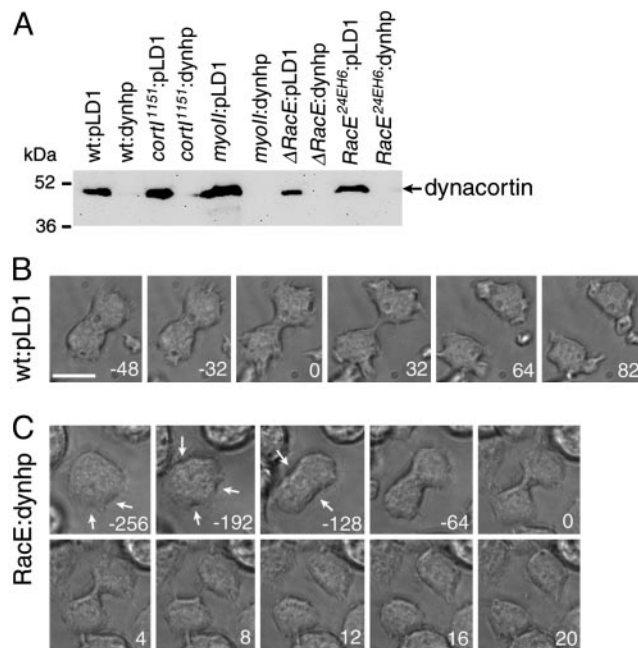


Fig. 2. *RacE/dynacortin* double mutants show uncontrolled cell morphology. (A) Western analysis by using anti-dynacortin antibodies indicates that *dynhp* significantly reduces dynacortin levels in all genetic backgrounds, wild type, *cort1*¹⁵¹, *myosin II*, Δ *RacE*, and *RacE*^{24E}. (B) Time series of micrographs of a wild-type cell undergoing division. The time series was taken from Movie 1. (C) Δ *RacE:dynhp* cells have altered cytokinesis dynamics. The cell attempts multiple furrows (arrows) before committing to a single cleavage plane at -128 s . The furrow ingresses slowly, then a rapid decrease is observed between 0 and 8 s. Movie frames come from Movie 3. Numbers in B and C are time in seconds. Time 0 is when D_x was reached. (Scale bar: $10 \mu\text{m}$.)

hairpin construct (*dynhp*; Fig. 2A) (15). The mutant strain data were rescaled through the same scheme as for the wild type. These mutants showed a nonlinear, triphasic trajectory characterized by a slow phase, followed by a more rapid thinning phase and then a final phase where the intercellular bridge dwelled for a period before severing (Fig. 7 B, C, and G, which is published as supporting information on the PNAS web site). D_x occurs at the transition between the slow and fast phases, and the transition was especially apparent in the *RacE* mutants (Fig. 7 C and G). We combined the first two phases into a “prebridge phase” and considered the final bridge-dwelling phase as a separate entity.

Because wild-type, *RacE*, and *dynacortin* lines displayed fundamentally different trajectories, we created a metric for direct comparison between each strain. We defined an apparent velocity as the speed with which the furrow diameter thinned from $2 \cdot D_x$ to $0.1 \cdot D_x$. We determined the time required to traverse $2 \cdot D_x$ to $0.1 \cdot D_x$, then calculated an apparent velocity by dividing $1.9 \cdot D_x$ by the time required to traverse that distance. For wild-type cells, the apparent velocity was $0.022 \mu\text{m/s}$. For the prebridge phase, *RacE* and *wt:dynhp* cells displayed similar apparent velocities as the wild-type cells (Fig. 7; see also Table 1, which is published as supporting information on the PNAS web site). Thus, the wild type and *RacE* and *dynacortin* mutants use different trajectories to achieve similar overall apparent velocities. The trajectories of the *RacE* mutant strains were rescued by the introduction of GFP-*RacE* (Fig. 7 D and H and Table 1).

When we silenced dynacortin in the *RacE* mutant backgrounds, the apparent velocity was significantly increased as compared with wild-type cells (Figs. 2 A and C, 3B, and 7 E and I, and Table 1). The Δ *RacE:dynhp* cells showed a single phenotypic class with a high apparent velocity ($0.089 \mu\text{m/s}$; Fig. 3B; see

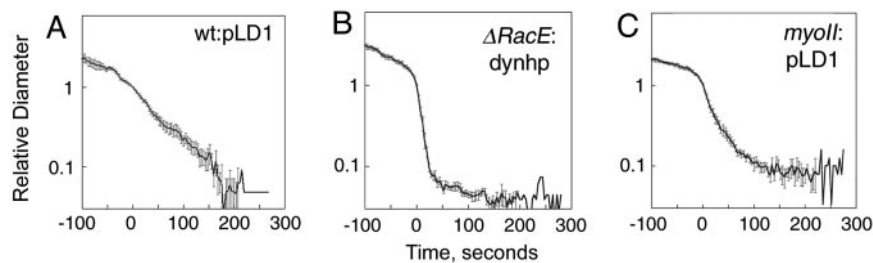


Fig. 3. Rescaling of the furrow diameter thinning data for each genetically modified strain of *Dictyostelium* cells. Each strain showed a distinct trajectory, depending on genotype. Error bars at each time point are standard errors of the mean. (A) Control wild-type cells carrying the empty vector pLD1. (B) Δ RacE:dynhp. (C) *Myosin II* mutant lines carrying pLD1. Composite of all data is shown in Fig. 7. Apparent velocities (v), rates (k), cross-over distances (D_x), and n values are presented in Table 1. To verify the success of the rescaling, nonaveraged data for these three graphs are shown in Fig. 6.

also Movie 3, which is published as supporting information on the PNAS web site). *RacE*^{24E}:dynhp double mutants displayed two classes of phenotypes, both of which demonstrate how RacE and dynacortin synergize to control cell shape during cytokinesis. One class showed a high apparent velocity (0.096 μ m/s), whereas the second class had a slower apparent velocity (0.035 μ m/s) and formed membrane blebs as the furrow ingressed (Fig. 7E and F; see also Movies 4 and 5, which are published as supporting information on the PNAS web site). Thus, a feedback mechanism may slow down furrow ingression if the plasma membrane ruptures from the cortex. Blebbing has been observed for nonadherent *RacE*^{24E} cells (14). Because nonadherent *Dictyostelium* have less polymeric actin (14), nonadherent *RacE*^{24E} and adherent *RacE*^{24E}:dynhp cells may have similarly altered cortical mechanics. When we averaged the fastest velocities from the steepest part of the curves of the individual raw data sets, the velocities were 0.31 ± 0.040 μ m/s ($n = 16$) for Δ RacE:dynhp and 0.19 ± 0.037 μ m/s ($n = 10$) for *RacE*^{24E}:dynhp with the fastest observed velocities at 0.74 μ m/s and 0.44 μ m/s for Δ RacE:dynhp and *RacE*^{24E}:dynhp, respectively. Thus, simultaneous removal of RacE and dynacortin caused up to a 30-fold (0.74 vs. 0.022) increase in furrow thinning velocity compared with the wild type. We propose that RacE and dynacortin regulate resistive stresses that slow furrow ingression; in essence, they provide a brake. Later, we present a simple, analytical model in which these resistive stresses account for the observed thinning dynamics.

Myosin II Mutant Furrow Thinning. Next, we investigated the role of myosin II in furrow thinning dynamics. The rescaling for *myosin II* mutants had to be modified because the dividing *myosin II* cell had a long cylindrical shape so that a crossover point was not immediately detectable. However, as the minimal furrow diameter decreased, the intercellular bridge was exposed that elongated similarly as the other strains. We fit this portion of the bridge-lengthening curve, extrapolated back to find D_x , and used this result to rescale the bridge-thinning trajectories. The *myosin II* mutants showed a similar nonlinear trajectory (Fig. 3C; see also Movie 6, which is published as supporting information on the PNAS web site). During the prebridge phase, the *myosin II* mutants had a slow phase followed by a faster phase with the transition again occurring at D_x . Silencing of dynacortin in the *myosin II*-null cells (*myoII*:dynhp) accelerated the apparent velocity of the prebridge phase nearly 2-fold without changing the fundamental furrow-thinning trajectory of the *myosin II*-null cells (Fig. 7L and Table 1; see also Movie 7, which is published as supporting information on the PNAS web site). Thus, the residual contractile mechanism of the *myosin II* mutants is slowed by the presence of dynacortin, supporting a role of dynacortin as a cytokinesis brake. When GFP-myosin II was expressed in the *myosin II* cells, the prebridge phase was converted into an exponential trajectory, and D_x was easily detected as in wild type (Fig. 7K and Table 1; see also Movie 8,

which is published as supporting information on the PNAS web site).

Global and Equatorial Actin Cross-Linking. Previously, we demonstrated that removal of either dynacortin or cortexillin-I from cells resulted in a softer cortex (15). Cortexillin-I concentrates in the cleavage furrow cortex, whereas dynacortin distributes in a complementary fashion to cortexillin-I during cytokinesis (19, 24). The carboxyl-terminal half of dynacortin (C181, sufficient for actin cross-linking) rescues the growth and cortical mechanics defects of *cortexillin-I* mutants (15). The *cortexillin I* mutant furrows thinned after a triphasic trajectory (Fig. 7M). Rescue with cortexillin I returns the thinning trajectory to an exponential (Fig. 7N). Interestingly, *cortexillin I* mutants rescued with dynacortin C181 showed a faster triphasic trajectory (Fig. 7O and Table 1). Although C181 rescues growth rate, furrow symmetry, crossover distance and cortical viscoelasticity, it does not rescue the furrow-thinning trajectory to an exponential (15). Thus, equatorial and global actin cross-linking proteins modulate furrow-thinning dynamics in distinct ways.

Model for Cytokinesis Dynamics. To evaluate the phase 2 furrow thinning dynamics, we compared the cell with a viscoelastic fluid. Two principal material properties that control the dynamics of viscoelastic fluids are the stretch modulus and viscosity (Supporting Appendix 1, which is published as supporting information on the PNAS web site). The stretch modulus (S_c) is the in-plane viscoelasticity of the cortex that is generated by the actin cytoskeleton and plasma membrane and is an energy cost for adding surface area to the cell. Because cells are viscoelastic fluids rather than elastic solids, the stretch modulus, similar to the surface tension of a liquid droplet, gives rise to a Laplace pressure that serves to minimize the surface area to volume ratio (25). Thus, during phase 1 of cytokinesis, the stretch modulus serves to resist the initial deformation of the cell. During phase 2, when a geometrically distinct intercellular bridge forms, the stretch modulus gives rise to a positive Laplace pressure difference ($P = 2S_c/R$ vs. $P = S_c/a$) between the bridge and the daughter cells (Fig. 4A and Supporting Appendix 1). The pressure difference tends to push cytoplasm from the bridge to speed up cytokinesis. For wild-type *Dictyostelium* cells, the stretch modulus (S_c) has been measured to be between 0.06 and 1.5 nN/ μ m, depending on time scale and whether the measurements were made by laser-tracking microrheology (LTM) or micropipette aspiration (MPA) (14, 15, 26) (K. D. Girard, S. C. Kuo, and D.N.R., unpublished data). Because the stretch modulus of the echinoderm egg cleavage furrow and the bending modulus of the mammalian cleavage furrow have been observed to increase as cytokinesis proceeds (9, 27–29), the Laplace pressure difference could be even larger than predicted from a uniform stretch modulus.

Viscosity is the energy cost for fluid flow and should slow

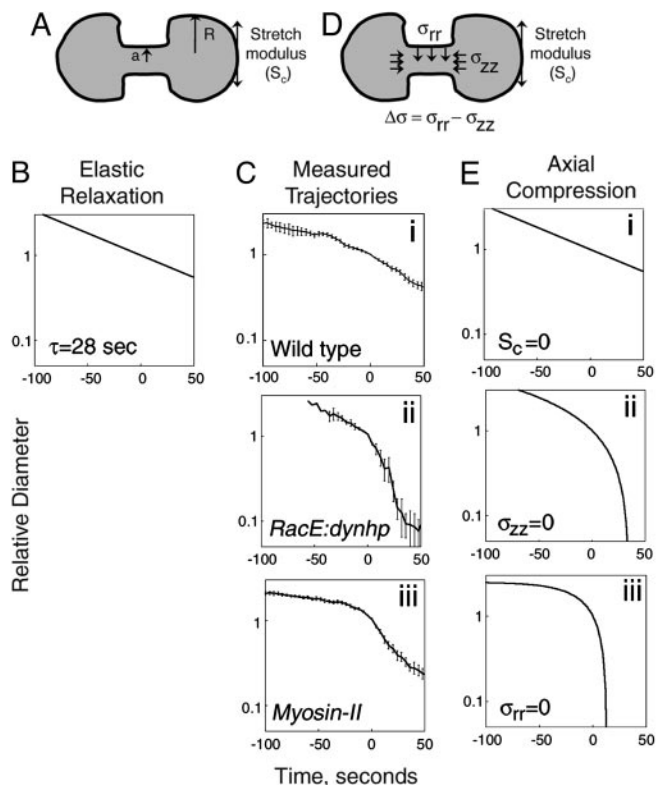


Fig. 4. Cylinder thinning model vs. measured furrow-thinning trajectories. (A) The viscoelasticity of the cell membrane and actin-rich cortex gives rise to a stretch modulus (S_c ; arrows tangent to the surface of the cell), which results in a positive Laplace pressure difference between the intercellular bridge (radius a) and daughter cells (radius R). (B) Cylinder thinning model with elastic relaxation (relaxation time $\tau = 28$ s). (C) Measured trajectories for wild type (i) and *RacE/dynacortin* (ii) and *myosin II* (iii) mutants. (D) Cylinder thinning model with contractile stress σ_{rr} (vertical arrows) and compressive stress σ_{zz} (horizontal arrows). $\Delta\sigma$ is the difference between σ_{rr} and σ_{zz} . (E) Furrow-thinning trajectories calculated by using the cylinder-thinning model. For all calculated trajectories, the cytoplasmic viscosity, μ , was assumed to be 0.35 nN·s/ μm^2 . (Ei) We assume compensation of the stretch modulus so that S_c approaches 1,000-fold less than the 1.5 nN/ μm measured by using MPA (14, 26) or 40-fold less than the S_c measured by using LTM (K. D. Girard, S. C. Kuo, and D.N.R., unpublished data) and $\Delta\sigma = 0.025$ nN/ μm^2 (see Fig. 9). (Eii) We assume the compressive stresses regulated by *RacE* and *dynacortin* are absent so that $\sigma_{zz} = 0$ nN/ μm^2 , $S_c = 0.02$ nN/ μm and $\Delta\sigma = 0.015$ nN/ μm^2 . From microaspiration and LTM studies, *RacE* and *dynacortin* mutants have 20% and 50% of wild-type S_c , respectively (14, 15). The S_c value used for *RacE/dynacortin* is justified from our LTM studies where on the seconds time scale (0.2 rad/s), wild-type S_c is 0.06 nN/ μm , wt: *dynhp* S_c is 0.02 nN/ μm , and S_c after latrunculin treatment of wild-type cells is 0.009 nN/ μm (K. D. Girard, S. C. Kuo, and D.N.R., unpublished data). Thus, these data bracket S_c for *RacE:dynhp* cells. Because of the rapid movements of *RacE* mutant cells, we cannot measure S_c for these cells by using LTM. (Eiii) We assume that radial stresses generated by myosin II are absent, so that $\sigma_{rr} = 0$, $\Delta\sigma = -0.08$ nN/ μm^2 , and $S_c = 0.1$ nN/ μm . Stretch modulus of *myosin II* mutant cells is based on LTM measurements (K. D. Girard, S. C. Kuo, and D.N.R., unpublished data).

down the cell shape change. Cytoplasmic viscosities (μ) are nonlinear, and for *Dictyostelium* range, from 10 to 350 Pa·s, depending on the applied force (30). As large-scale shape changes are likely to be dominated by the highest viscosity, the relevant viscosity for cytokinesis is likely to be 350 Pa·s (0.35 nN·s/ μm^2).

If one assumes that furrow thinning and bridge recoil are driven only by the stretch modulus and the resistance is due solely to viscous drag, then a dimensional analysis suggests the process occurs with a velocity proportional to S_c/μ that depends

on the geometry of the bridge (31, 32) (Supporting Appendix 1). For a cylindrical bridge, the proportionality factor is 1/3, yielding a velocity, $v = S_c/3\mu$. This ratio describes an entirely passive mechanism for the thinning of the cylindrical bridge and predicts that the wild-type furrow bridge ingression and bridge recoil after severing would achieve velocities in the 1.5 $\mu\text{m/s}$ range by using the largest stretch modulus and viscosity. For wild-type and mutant cells, the recoil of the intercellular bridge occurred with velocities in the 1–2 $\mu\text{m/s}$ range, indicating that recoil velocity, stretch modulus, and viscosity are consistent within a framework of $v = S_c/3\mu$ (Fig. 8 and Movie 9, which are published as supporting information on the PNAS web site).

The measured apparent velocity of wild-type furrow ingression is ≈ 70 -fold (1.5 $\mu\text{m/s}$ vs. 0.022 $\mu\text{m/s}$) slower than the predicted velocity. Further, the passive mechanism predicts a linear decrease rather than the exponential decay displayed by the wild-type cells. Therefore, the wild-type thinning dynamics are not driven solely by a passive mechanism.

To analyze the measured trajectories more quantitatively, we considered a simple analytical model of furrow thinning in which the intercellular bridge is modeled as a perfect cylinder (Supporting Appendix 1). We first considered whether bulk elasticity effects of the cleavage furrow cytoskeleton could control the furrow-thinning rates. However, a long time constant for elastic relaxation ($\tau = 28$ seconds) was required to match the measured wild-type dynamics (Fig. 4 B vs. Ci; Supporting Appendix 1, Eq. 18). Because the measured relaxation time constant for *Dictyostelium* is < 1 s (30), slowing of furrow thinning by elastic effects seems unlikely. More importantly, bulk elasticity effects, which only allow exponential decay, do not explain the mutant trajectories.

Next, we hypothesized that compressive stresses (σ_{zz}) exist at the two ends of the intercellular bridge and, hence, slow down cytokinesis (Fig. 4D and Supporting Appendix 1, Eq. 12). In addition, radial stresses (σ_{rr}) are actively generated at the surface of the cylindrical intercellular bridge and act to thin the bridge, speeding up cytokinesis. For a cylindrical bridge, the antagonistic effect of the radial and compressive stresses is characterized simply by the stress difference ($\Delta\sigma = \sigma_{rr} - \sigma_{zz}$). The hypothesis of the model is that axial compression acts on the ends of the furrow to cancel the Laplace pressure, slowing the flow of cytoplasm out of the bridge so that the decay is controlled by the myosin II-driven radial stresses. Importantly, these compressive stresses do not need to be generated precisely at the ends of the furrow. Rather, they may be generated by the viscoelasticity of the daughter cell cortical cytoskeleton or cytoplasm, producing resistance vectors that sum to vectors that counteract flow from the bridge. Setting the viscosity, μ , to 0.35 nN·s/ μm^2 , the cylinder thinning model produced furrow thinning trajectories, which are in good agreement with those observed for the mutants (Fig. 4 Cii and Ciii vs. Eii and Eiii). The parameters for $\Delta\sigma$ and S_c (given in the Fig. 4 legend), which were used to obtain the calculated trajectories, are reasonable given available measured values (14, 15). The *RacE/dynacortin* mutant trajectory was best modeled by allowing the stretch modulus and a positive $\Delta\sigma$ to drive furrow ingression, consistent with the idea that these proteins slow furrow thinning by providing a brake, which counteracts the Laplace pressure. Consistent with the idea that myosin II generates the active radial stresses, the *myosin II* mutant dynamics are recapitulated if we set σ_{rr} to 0 so that $\Delta\sigma$ is negative. Thus, the major distinction between the mutants was that *RacE/dynacortin* mutants required a positive $\Delta\sigma$, whereas the *myosin II* mutants required a negative $\Delta\sigma$. Both sets of mutants had furrow-thinning trajectories that accelerated near D_x , consistent with D_x representing the point when the stretch modulus strongly favors furrow thinning.

To obtain exponential decay furrow-thinning dynamics, we propose that *RacE* and *dynacortin*-generated compressive

stresses counteract the effects of the stretch modulus. This balance creates the exponential decay observed for wild-type cytokinesis when the measured rate constant k (-0.012 s^{-1}) for wild-type thinning was used to calculate the stress difference ($\Delta\sigma$) between the radial and compressive stress ($-k = \Delta\sigma/6\mu$; $\Delta\sigma = 0.025 \text{ nN}/\mu\text{m}^2$) (Fig. 4 *Ci* vs. *Ei*). Clearly, changes in the viscosity can also impact the dynamics of bridge thinning; we present several calculated trajectories where stretch modulus and viscosity are varied to demonstrate how these parameters might contribute to the trajectory (Fig. 9, which is published as supporting information on the PNAS web site).

Using the values obtained from the dynamics analysis, we estimated the amount of radial stresses generated by myosin II and relate that to actual amounts of myosin II present in the cleavage furrow cortex (*Supporting Appendix 2*, which is published as supporting information on the PNAS web site). Using the stress difference from wild-type cells and the compressive stresses that account for the *myosin II* mutant furrow-thinning dynamics (Fig. 4*E*), the active radial stresses ($\sigma_{rr} = \Delta\sigma + \sigma_{zz}$) are $\approx 0.1 \text{ nN}/\mu\text{m}^2$. The actual amounts of myosin II present in the furrow around D_x are predicted to generate radial stresses that closely agree with the observed stresses from the dynamics analysis (6). In short, wild-type thinning dynamics are exquisitely controlled by RacE and dynacortin and are largely driven by active myosin II-generated radial stresses.

Discussion

Two broadly defined mechanical models, polar relaxation and equatorial contractility, have dominated the cytokinesis field in recent decades (18). The polar relaxation model ascribes expansive forces to the polar cortex. An increase in the viscoelasticity of the cleavage furrow cortex then guides cleavage furrow ingression (9, 27–29). In the equatorial contractility model, equatorial myosin II ATPase generates the cleavage forces (2–4). Although these two classic models are invaluable for generating a framework for relating proteins to the mechanics of cytokinesis, they are inherently limited as they are unnecessarily dichotomous and are nondynamical. Our data support a model in which both global and equatorial proteins interact to control the dynamics of furrow ingression.

To create a quantitative framework for cytokinesis, we developed a simple analytical model in which the phase 2 dividing cell is compared with a simple viscoelastic fluid. The rationale for the proposed model was that the number of parameters (myosin II mechanochemistry, a Laplace pressure, resistive stresses, and viscosity) should be minimized and that the parameters should be largely experimentally verifiable. These restrictions limit the model because it is not completely molecular and does not allow the values of stretch modulus, viscosity, or active and compressive stresses to vary temporally or spatially as furrow-thinning proceeds. Although this model is clearly simplified, it is physically grounded and appropriate given current available experimental data.

From the analysis, it becomes clear that wild-type cells behave very differently from viscoelastic fluids. In contrast, *myosin II* and *RacE/dynacortin* mutant cytokineses have furrow-thinning trajectories that are much easier to reconcile from fluid mechanical considerations and the available measured physical parameters. Wild-type furrow-thinning trajectories are more difficult to reconcile, perhaps because wild-type cells have more contractile mechanisms at their disposal than the mutants have.

Two classes of stretch modulus values have emerged from MPA and LTM. MPA yields a wild-type S_c of $1.5 \text{ nN}/\mu\text{m}$, whereas LTM yields a wild-type S_c of $0.06 \text{ nN}/\mu\text{m}$ (at 0.2 rad/s), producing a 25-fold (1.5 vs. 0.06) discrepancy (14, 15, 26). In contrast, measured stretch modulus values for *myosin II* mutants are $0.5 \text{ nN}/\mu\text{m}$ from MPA (ref. 24; J. C. Effler, P. Iglesias, and D.N.R., unpublished data) and 0.1 – $0.2 \text{ nN}/\mu\text{m}$ from LTM (K. D.

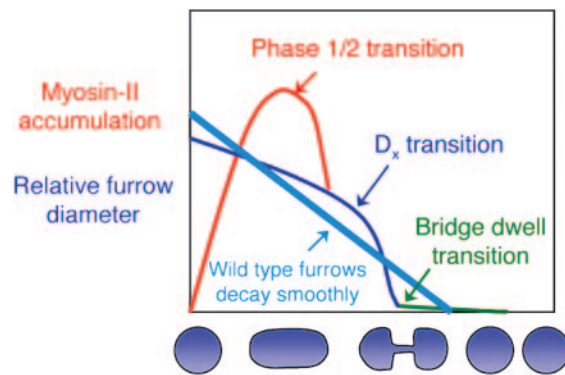


Fig. 5. Three mechanical transitions of cleavage furrow contractility. Wild-type cells pass smoothly through each transition, leading to bridge severing.

Girard, S. C. Kuo, and D.N.R., unpublished data), yielding only a 3–5-fold discrepancy for this genotype and ruling out systematic differences in the two methods. These results beg the question as to what these parameters indicate about cortical mechanics. Interestingly, the LTM-derived values readily account for the furrow-thinning dynamics, whereas the MPA-derived values account for the bridge recoil. Previously, we showed that the amount of myosin II at the furrow cortex at the phase 1/2 transition is predicted by using MPA values (6), whereas the myosin II amount present at the time of D_x is predicted from the dynamics analysis by using LTM-derived values (*Supporting Appendix 2*). Because MPA measures long-range mechanics (several micrometer range) and LTM measures short-range mechanics (low micrometer range), phase 1 cytokinesis may be dominated by long-range mechanics and phase 2 may be controlled by short-range mechanics (25). Bridge recoil occurs over several microns, and given its high velocity, it may again be dominated by long-range mechanics. Thus, RacE- and dynacortin-created compressive stresses may only need to counteract a 40-fold difference in Laplace pressure rather than a 1,000-fold difference (compare Fig. 9 *A* vs. *D* and *F* vs. *D*).

How RacE and dynacortin generate compressive stresses to slow cytokinesis becomes a fundamental question for understanding the control of cytokinesis dynamics. These proteins may modulate the cortical and/or cytoplasmic viscoelasticity of the daughter cells. The viscoelasticity of the daughter cells may generate resistive (compressive) stresses that slow furrow thinning. A prediction from the model then is if the compressive stresses could be alleviated perhaps by micromanipulation, then furrow thinning should accelerate. Another mechanical parameter to consider is the mechanical phase angle ($\tan^{-1}(\text{viscous modulus/elastic modulus})$). Myosin II increases the phase angle, making the cortex more liquid-like (viscous), whereas dynacortin reduces the phase angle, making the cortex more solid-like (elastic) (15) (K. D. Girard, S. C. Kuo, and D.N.R., unpublished data). This and other data indicate that dynacortin and myosin II have opposite effects on cortical mechanics. Because dynacortin and myosin II have complementary distributions in dividing wild-type cells, these two proteins probably control cytokinesis dynamics by modulating cortical mechanical properties in an antagonistic manner.

In summation, our analysis suggests a picture for cleavage furrow contractility that has three mechanical transitions (Fig. 5). The first transition occurs between phase 1 and phase 2, corresponding to the point when the maximum amount of myosin II localizes at the cleavage furrow (6). Because *myosin II* mutant *Dictyostelium* divide on surfaces, crawling forces help elongate the cell during phase 1; indeed, nonadherent *myosin II* mutants fail to elongate during phase 1 (7). We suggest that the

Supplementary Table 1. Apparent velocity and cross-over distance for each strain

Strain	Apparent velocity, v ($\mu\text{m/s}$)	Furrow thinning rate, k (s^{-1})	Cross-over length, D_x (μm)*	n
Wild type: pLD1	0.022	-0.012	2.7 \pm 0.13	26
Wild type: dynhp	0.021		1.5 \pm 0.20	14
ΔRacE : pLD1	0.029		1.8 \pm 0.070	14
ΔRacE :GFPRacE	0.024	-0.017	2.3 \pm 0.12	11
ΔRacE : dynhp	0.089		3.0 \pm 0.22	25
RacE^{24E} : pLD1	0.018		2.8 \pm 0.16	6
RacE^{24E} : GFPRacE	0.024	-0.018	2.2 \pm 0.27	9
RacE^{24E} : dynhp (Nonblebbers)	0.096		4.0 \pm 0.51	7
RacE^{24E} : dynhp (Blebbers)	0.035		2.9 \pm 0.26	9
<i>Myosin-II</i> : pLD1	0.020		1.9 \pm 0.095	19
<i>Myosin-II</i> : GFPmyosin-II	0.025	-0.012	2.4 \pm 0.15	16
<i>Myosin-II</i> : dynhp	0.035		2.4 \pm 0.12	15
<i>cortI</i> ¹¹⁵¹ : pLD1	0.022		2.2 \pm 0.19	16
<i>cortI</i> ¹¹⁵¹ : cortexillin-I	0.025	-0.016	2.5 \pm 0.068	6
<i>cortI</i> ¹¹⁵¹ : C181	0.029		3.0 \pm 0.14	19

*All values are Mean \pm SEM.

Supplementary Figure 6. Non-averaged, rescaled furrow thinning trajectory data for A. wt:pLD1, B. $\Delta RacE$:dynhp and C. *myoII*:pLD1 cells.

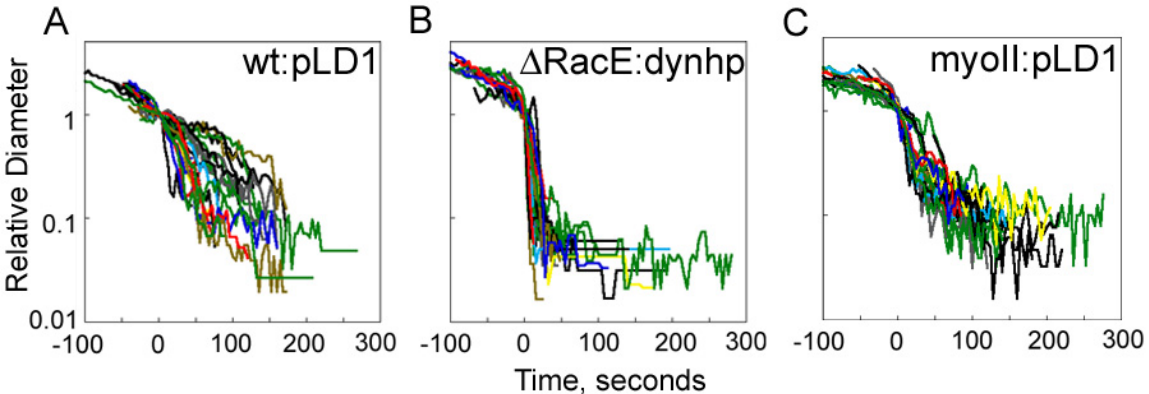
Supplementary Figure 7. Global and equatorial proteins influence cleavage furrow thinning dynamics. A. Control wild type cells carrying the empty vector pLD1. B. Wild type cells expressing a *dynacortin* hairpin (dynhp) construct. C-E. $RacE^{24E}$ lines carrying C. pLD1, D. GFP*RacE*, or E. dynhp. $RacE^{24E}$:dynhp data set for the non-blebbing class. F. $RacE^{24E}$:dynhp data set for the class of cells that formed membrane blebs during cytokinesis. G-I. $\Delta RacE$ lines carrying G. pLD1, H. GFP*RacE* or I. dynhp. The trace is the composite of all cells from this line as no cells were observed to form blebs during division. J-L. *Myosin-II* mutant lines carrying J. pLD1, K. GFP*myosin-II* or L. dynhp. M-O. *Cortexillin-I* mutant lines carrying M. pLD1, N. cortexillin-I or O. dynacortin C181 expression plasmids. Apparent velocities (v), rates (k), cross-over distances (D_x) and n-values are presented in Supplementary Table 1. This composite of data represents more than 20,000 measurements from 212 cells.

Supplementary Figure 8. Bridge recoil occurs at high velocities similar to those predicted from the passive material properties. A. Time series of a recoiling bridge after being severed. The genotype of this cell is *myo-II*: pLD1. Time, sec. Scale bar, 10 μ m. B. A plot of the lengthening and recoil after severing of the furrow bridge. The intercellular bridge lengthens linearly with time and then upon severing, recoils rapidly. At some point, the recoiling bridge is slowed down and is subsequently withdrawn with a velocity in the range of the original bridge lengthening. This particular data set was acquired from a wt:pLD1 cell.

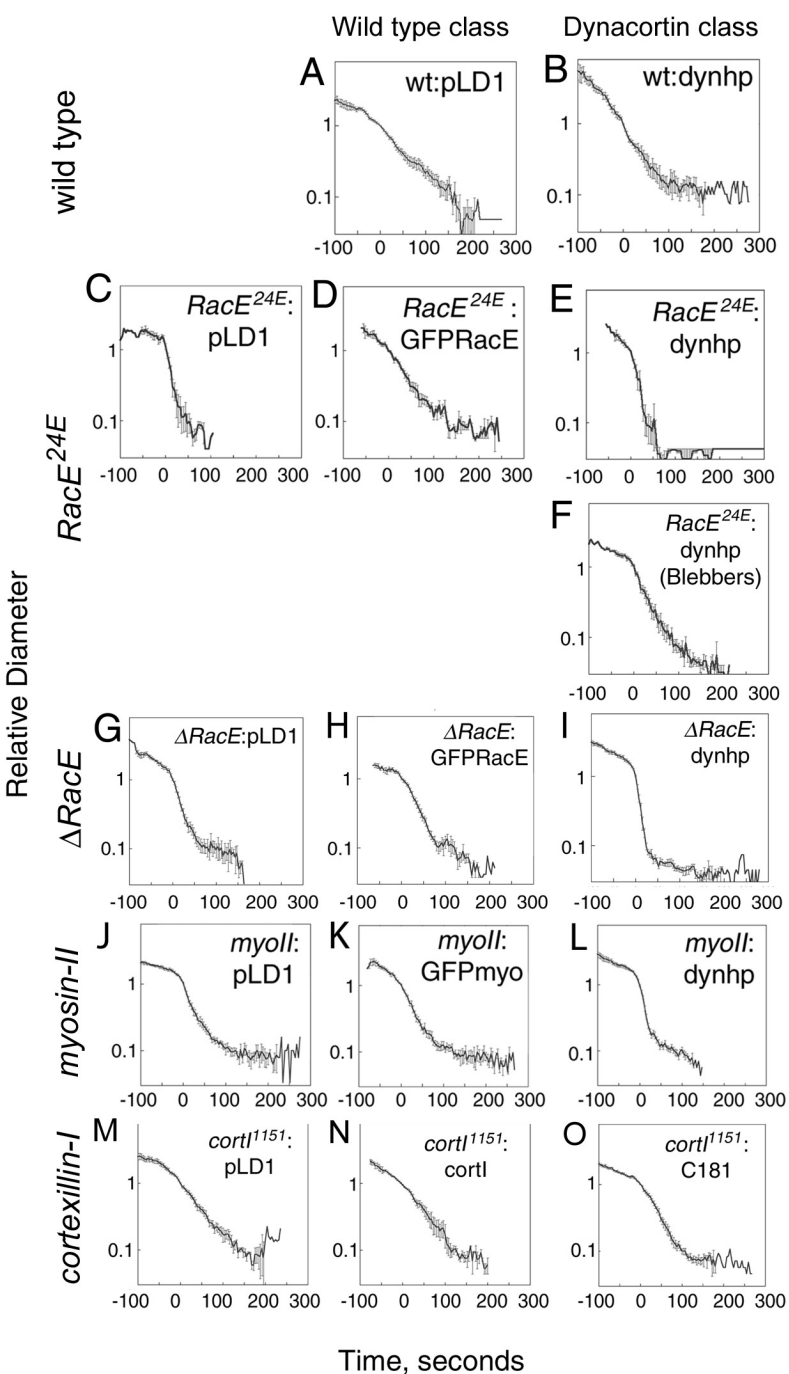
Supplementary Figure 9. Varying stretch modulus or viscosity alters the furrow thinning trajectory. Trajectories were calculated using the axial compression model (Equation 12). Parameters were varied to show how varying S_c and viscosity change the trajectory. A. S_c was based on wild type stretch modulus measured using micropipette aspiration (1, 2). We have verified this value of 1.5 nN/ μm in our own laboratory (Effler, Iglesias, and Robinson, unpublished). Viscosity was the highest measured (3). B. Ten-fold reduction in S_c . C. 100-fold reduction in S_c . D. 1000-fold reduction in S_c . E. Ten-fold increase in viscosity. F. S_c was based on the wild type stretch modulus (at 0.2 rad/sec) measured using laser tracking microrheology (Girard, Kuo and Robinson, unpublished). G. Five-fold increase in viscosity. H. 10-fold increase in viscosity. Units for stretch modulus, S_c (nN/ μm) and viscosity, μ (nN•s/ μm^2). $\Delta\sigma$ was 0.025 nN/ μm^2 , the value measured from the wild type thinning trajectory.

References

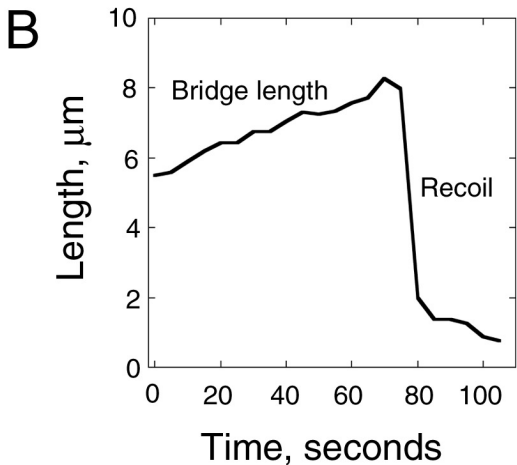
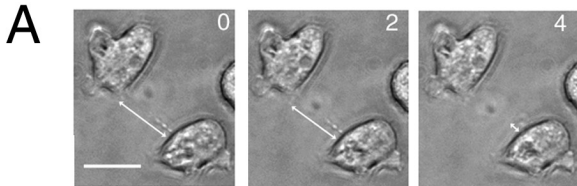
1. Dai, J., Ting-Beall, H. P., Hockmuth, R. M., Sheetz, M. P. & Titus, M. A. (1999) *Biophys. J.* **77**, 1168-1176.
2. Gerald, N., Dai, J., Ting-Beall, H. P. & DeLozanne, A. (1998) *J. Cell Biol.* **141**, 483-492.
3. Feneberg, W., Westphal, M. & Sackmann, E. (2001) *Eur Biophys J* **30**, 284-294.



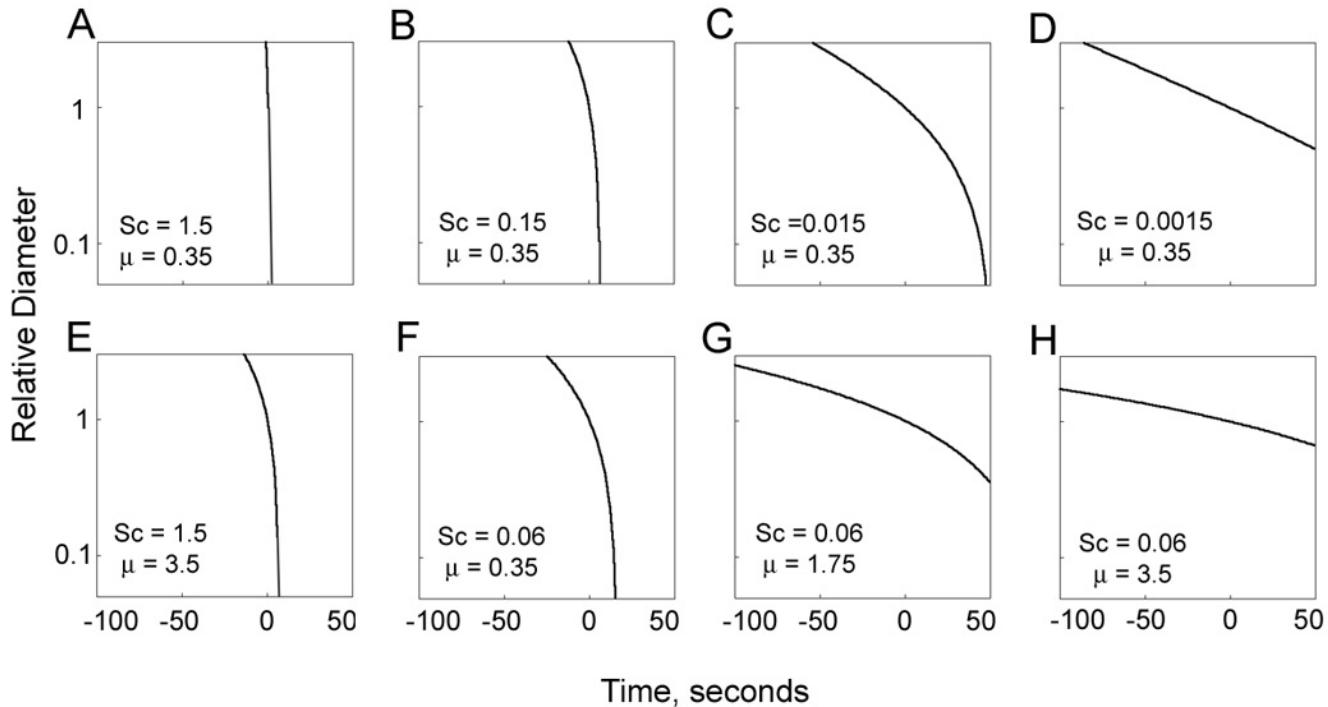
Supplementary Figure 6



Supplementary Figure 7



Supplementary Figure 8



Supplementary Figure 9

Supplementary Movies

Supplementary Movie 1: Wild type:pLD1 cell undergoing cytokinesis.

Supplementary Movie 2: Wild type:pLD1 cell undergoing cytokinesis.

Supplementary Movie 3: $\Delta RacE$:dynhp cell undergoing cytokinesis.

Supplementary Movie 4: $RacE^{24E}$:dynhp cell undergoing cytokinesis.

Supplementary Movie 5: $RacE^{24E}$:dynhp cell undergoing cytokinesis. The cell forms many membrane blebs during cytokinesis.

Supplementary Movie 6: *MyoII*:pLD1 cell undergoing cytokinesis.

Supplementary Movie 7: *MyoII*:dynhp cell undergoing cytokinesis.

Supplementary Movie 8: *MyoII*:GFPmyosin-II cell undergoing cytokinesis.

Supplementary Movie 9: Recoil of the bridge after severing of a *myoII*:pLD1 cell.

All movies are collected at 2-sec intervals with a resolution of 0.2 $\mu\text{m}/\text{pixel}$. Movies are played at 10-frames/sec.

Supporting Appendix 1: Cylinder Thinning Model

Here, we give a detailed derivation of our analytic model for the thinning dynamics of the intracellular bridge during the last stage of cytokinesis. This model is a simple extension of the model first used by Entov and Hinch (1) to describe elastic effects in the thinning of a polymeric liquid bridge. We begin by approximating the intercellular bridge as a perfect cylinder of radius $a(t)$. The cortical stretch modulus, S_c , gives rise to a Laplace pressure across the cortex, which is proportional to the mean curvature. For a sphere of radius R , the Laplace pressure is

$$P = \frac{2}{R} S_c. \quad [1]$$

For a cylinder, the Laplace pressure is

$$P = \frac{S_c}{a}. \quad [2]$$

If we approximate the two daughter cells as perfect spheres and the bridge as a perfect cylinder, we find the Laplace pressure P is larger inside a 1- μm radius bridge than the 4- μm radius daughter cells, thus the Laplace pressure tends to squeeze materials from the bridge into the two daughter cells. If we associate a viscosity μ with flow of the material from the bridge into the daughter cells, then dimensional analysis gives a characteristic velocity U_* for the outflow

$$U_* = \frac{S_c}{\mu}. \quad [3]$$

In the rest of the appendix, we derive simple, analytic expressions, which describe bridge-thinning dynamics precisely, provided the geometry of the furrow remains cylindrical. We consider two extreme scenarios. First, we examine the thinning dynamics driven by a contractile radial stress exerted by myosin II, which acts against compressive stresses from the two daughter cells. This thinning dynamics is a combination of a linear decrease and an exponential decay, with the exponential decay preceding the linear decrease. Second, we examine the thinning dynamics associated with elastic stresses associated with materials inside the intercellular bridge. Here, a dominance of elastic stresses results in an exponential decay. In both cases, we retain the stretch modulus S_c in the analysis.

For the first scenario, we begin with volume conservation. As the cylinder thins and lengthens, volume conservation requires that the decrease in volume due to radial thinning in a volume element with length Δz in the cylinder, $\partial / \partial t (\pi a^2 \Delta z)$, is balanced by volume flux, $-(\pi a^2 U_z)|_z^{z+\Delta z}$, out of the two ends of the same volume element. Here U_z denotes the axial velocity inside the cylinder. Simplifying the expression and taking the limit of Δz going to 0, we obtain

$$\frac{\partial a}{\partial t} = -\frac{1}{2} \frac{\partial U_z}{\partial z} a(t) = -\frac{1}{2} e(t) a(t), \quad [4]$$

where the axial strain rate $e(t)$ is unknown. In addition to volume conservation, the viscous flow in the thinning bridge must satisfy boundary conditions on the cylinder surface and at the two ends of the cylinder. These are the conditions that the fluid stresses should be continuous across a fluid interface. The full expression can be found in any textbook on fluid mechanics (2). Because of the extreme simplicity of the bridge geometry, the boundary conditions reduce to radial stress balance across the cylinder and axial stress balance across the ends of the cylinder. The radial stress balance has the form

$$\sigma_{rr} + \frac{S_c}{a} = P - 2\mu \frac{\partial U_r}{\partial r} = P + \mu e(t), \quad [5]$$

where σ_{rr} is the actively generated radial stress on the bridge surface, P is the fluid pressure and U_r is the radial velocity. We also assume σ_{rr} is entirely contractile, corresponding to a radial force exerted inwards. In arriving at the right hand side of **5**, we made use of the fact that the velocity field should be incompressible, so that

$$\frac{1}{r} \frac{\partial}{\partial r} (rU_r) + \frac{\partial U_z}{\partial z} = 0, \quad [6]$$

which relates the radial derivative of U_r to the axial derivative of U_z . In our problem, **6** is simply

$$\frac{1}{r} \frac{\partial}{\partial r} (rU_r) + e(t) = 0. \quad [7]$$

Integrating **7** with respect to r , we find

$$U_r = -\frac{e(t)r}{2} - \frac{c_0}{r}. \quad [8]$$

Because the centerline radial velocity U_r ($r = 0$) must be bounded, $c_0 = 0$. This finding means $\partial(U_r)/\partial r = -e(t)/2$, hence the right hand side of Eq. **5**.

At the end of the cylindrical bridge, where the bridge joins onto a daughter cell, the axial stress balance takes the form

$$-\sigma_{zz} = -P + 2\mu e(t), \quad [9]$$

where σ_{zz} is the compressive axial stress exerted by the daughter cell at the ends of the cylinder. If we take **9** as an equation for the pressure and substitute it into Eq. **5**, we then obtain the following expression for the axial strain rate $e(t)$

$$e(t) = \frac{S_c}{3\mu a(t)} + \frac{\sigma_{rr} - \sigma_{zz}}{3\mu}. \quad [10]$$

Substituting **10** into **4** yields

$$\frac{\partial a}{\partial t} = -\frac{S_c}{6\mu} - \frac{(\sigma_{rr} - \sigma_{zz})}{6\mu} a(t). \quad [11]$$

Note if $\sigma_{rr} = \sigma_{zz} = 0$, then $a(t) = a_0 - (S_c/6\mu) t$. The radius thins linearly over time with a characteristic velocity proportional to U_* , consistent with the earlier dimensional analysis.

Now suppose both of the applied stresses are constant over the time, **11** can be integrated to yield

$$a(t) = a_0 e^{-(\Delta\sigma)/6\mu} - \frac{S_c}{\Delta\sigma} (1 - e^{-(\Delta\sigma)/(6\mu)}), \quad [12]$$

where $\Delta\sigma = \sigma_{rr} - \sigma_{zz} > 0$ and we have used the initial condition $a(t=0)=a_0$. Eq. **12** describes a thinning dynamics which is a combination of linear decrease and exponential decay. The linear decrease component can be seen most easily by considering the situation where $\Delta\sigma/(6\mu)$ is small. In that case, Taylor expansion of **12** shows that the bridge thinning dynamics reduces to a linear thinning at leading order, as

$$a(t) = a_0 - \frac{S_c}{6\mu} t + \frac{S_c \Delta\sigma}{72\mu^2} t^2 + \dots \quad [13]$$

Here, the effect of the applied stress enters only as a correction to the linear dynamics. In short, depending on the magnitude of $\Delta\sigma$, the thinning dynamics changes continuously from a linear decrease to an exponential thinning. One trend, however, is robust and does not depend on the magnitude of $\Delta\sigma$: the dynamics always looks more exponential at the beginning, when $a(t)$ is large. As $a(t)$ decreases, the linear decrease becomes more obvious.

We now turn to the second scenario: the buildup of elastic stresses inside the thinning bridge. We begin with the simplest possible model of elastic effects. The material in the bridge is assumed to be isotropic and that the deformation lies within the linear elasticity regime. More precisely, we assume that the deformation is purely an axial stretch, denoted by A_z , and behaves as

$$\frac{\partial A_z}{\partial t} = 2e(t)A_z(t) - \frac{A_z(t)}{\tau}, \quad [14]$$

where τ is an elastic relaxation time. Using Eq. 4 to substitute for $e(t)$ in 14 and after rearrangement, we find 14 can be rewritten as

$$\frac{\partial}{\partial t} [\ln(A_z)] = -4 \frac{\partial}{\partial t} [\ln(a(t))] - \frac{1}{\tau}. \quad [15]$$

Upon integrating 15 with respect to t and using the initial condition $A_z(t=0) = 1$, we find

$$A_z = \left(\frac{a_0}{a(t)} \right)^4 e^{-t/\tau}. \quad [16]$$

To get $a(t)$, we assume in addition that the elastic stress is sufficiently large so that the viscous stress associated with flow inside the bridge is negligible in comparison. In other words, the elastic stress completely balances the Laplace pressure due to the surface stretch modulus

$$\frac{S_c}{a(t)} = g A_z(t), \quad [17]$$

where g is the elastic modulus. Substituting 16 into 17 yields

$$a(t) = a_0 \left(\frac{a_0}{S_c} g e^{-t/\tau} \right)^{1/3}. \quad [18]$$

The bridge radius decays as a near exponential with the characteristic decay time given by the relaxation time of the elastic stresses. Note in arriving at 18 we have simplified the dynamics considerably. A more complete treatment, which considers the dynamics at earlier times where viscous stresses are comparable with elastic stresses, can be found in Entov and Hinch (1). They found that when both effects are considered, the thinning dynamics first appears linear and, then, approaches an exponential decay as $a(t)$ becomes small.

Eqs. 12 and 18 were used to compare theoretical furrow thinning dynamics to observed furrow-thinning dynamics for wild-type and mutant cytokineses in Fig. 4.

1. Entov, V. M. & Hinch, E. J. (1997) *J. Non-Newtonian Fluid Mech.* **72**, 31-53.
2. Batchelor, G. K. (1967) *An Introduction to Fluid Mechanics* (Cambridge Univ. Press, Cambridge, U.K.).

Supporting Appendix 2

From the kinetics analysis of furrow thinning from wild-type and *myosin II* mutant cells, we can now determine the amount of active radial stress generated by myosin II in the cleavage furrow.

From the wild-type furrow-thinning decay rate ($k = -0.012 \text{ s}^{-1}$) and viscosity ($\mu = 0.35 \text{ nN}\cdot\text{s}/\mu\text{m}^2$; ref. 1):

$$k = \frac{-\Delta\sigma}{6\mu} \quad [1]$$

$$\Delta\sigma = 0.025 \text{ nN}/\mu\text{m}^2$$

To determine the σ_{rr} generated by myosin II, we use the resistive stresses ($\sigma_{zz} = 0.08 \text{ nN}/\mu\text{m}^2$) that account for the furrow-thinning dynamics observed in the *myosin II* mutant cells.

$$\Delta\sigma = \sigma_{rr} - \sigma_{zz} . \quad [2]$$

$$\sigma_{rr} = \Delta\sigma + \sigma_{zz} . \quad [3]$$

Thus, the radial stresses generated by myosin II are

$$** \sigma_{rr} = 0.1 \text{ nN}/\mu\text{m}^2.$$

This value can be compared with the amount of myosin II found in the cleavage furrow. From our previous quantification (2), there are $\approx 60,000$ myosin II motor domains in the cleavage furrow at the time of D_x .

Therefore, the number of heads•force/head•duty ratio (see ref. 2 and references therein for explanation of the chosen values) of *Dictyostelium* myosin II provides the force F :

$$F = \approx 60,000 \text{ heads} \cdot 3 \text{ pN/head} \cdot 0.6\% = 1 \text{ nN} \quad [4]$$

The surface area (SA) of the furrow at wild-type $D_x = 2.7 \mu\text{m}$ is

$$SA = \pi dl = 23 \mu\text{m}^2 \text{ where } d = l = D_x. \quad [5]$$

Thus, the radial stress (F/SA ; $1 \text{ nN}/23 \mu\text{m}^2$) predicted from myosin II amounts are

$$** \sigma_{rr} = 0.04 \text{ nN}/\mu\text{m}^2.$$

**Thus, the radial stresses ascribed to myosin II from the kinetics analysis agree closely with the radial stresses predicted from the actual amounts of myosin II in the furrow.

1. Feneberg, W., Westphal, M. & Sackmann, E. (2001) *Eur. Biophys. J.* **30**, 284-294.
2. Robinson, D. N., Cavet, G., Warrick, H. M. & Spudich, J. A. (2002) *BMC Cell Biol.* **3**, 4.